

Optimizing modelling in iterative image reconstruction for preclinical pinhole PET

This content has been downloaded from IOPscience. Please scroll down to see the full text.

2016 Phys. Med. Biol. 61 3712

(<http://iopscience.iop.org/0031-9155/61/10/3712>)

View [the table of contents for this issue](#), or go to the [journal homepage](#) for more

Download details:

IP Address: 143.121.222.169

This content was downloaded on 20/04/2016 at 17:30

Please note that [terms and conditions apply](#).

Optimizing modelling in iterative image reconstruction for preclinical pinhole PET

Marlies C Goorden¹, Jarno van Roosmalen¹,
Frans van der Have^{1,2} and Freek J Beekman^{1,2,3}

¹ Section of Radiation Detection and Medical Imaging, Applied Sciences,
Delft University of Technology, Mekelweg 15, 2629 JB Delft, The Netherlands

² MILabs B.V., Utrecht, Heidelberglaan 100 STR 4.105, 3584 CX, The Netherlands

³ Department for Translational Neuroscience, Brain Center Rudolf Magnus,
University Medical Center Utrecht 3584 CG, Utrecht, The Netherlands

E-mail: m.c.goorden@tudelft.nl

Received 9 October 2015, revised 4 March 2016

Accepted for publication 16 March 2016


Published 19 April 2016



Abstract

The recently developed versatile emission computed tomography (VECTor) technology enables high-energy SPECT and simultaneous SPECT and PET of small animals at sub-mm resolutions. VECTor uses dedicated clustered pinhole collimators mounted in a scanner with three stationary large-area NaI(Tl) gamma detectors. Here, we develop and validate dedicated image reconstruction methods that compensate for image degradation by incorporating accurate models for the transport of high-energy annihilation gamma photons. Ray tracing software was used to calculate photon transport through the collimator structures and into the gamma detector. Input to this code are several geometric parameters estimated from system calibration with a scanning ^{99m}Tc point source. Effects on reconstructed images of (i) modelling variable depth-of-interaction (DOI) in the detector, (ii) incorporating photon paths that go through multiple pinholes ('multiple-pin-hole paths' (MPP)), and (iii) including various amounts of point spread function (PSF) tail were evaluated. Imaging ¹⁸F in resolution and uniformity phantoms showed that including large parts of PSFs is essential to obtain good contrast-noise characteristics and that DOI modelling is highly effective in removing deformations of small structures, together leading to 0.75 mm resolution PET images of a hot-rod Derenzo phantom. Moreover, MPP modelling reduced the level of background noise. These improvements were also clearly visible in mouse images. Performance of VECTor can thus be significantly improved by accurately modelling annihilation gamma photon transport.

Keywords: image reconstruction, positron emission tomography (PET), single photon emission computed tomography (SPECT)

 Online supplementary data available from stacks.iop.org/PMB/61/3712/mmedia

(Some figures may appear in colour only in the online journal)

1. Introduction

High-resolution single photon emission computed tomography (SPECT) and positron emission tomography (PET) imaging of small experimental animals is key in the development of new pharmaceuticals and tracers and the study of physiology and disease (Weissleder *et al* 2010). Recently, simultaneous high-resolution PET and SPECT have been enabled by a newly developed Versatile Emission Computed Tomography system (VECTor, (Goorden *et al* 2013, Miwa *et al* 2015)). Today VECTor can perform 0.5 mm ^{99m}Tc -SPECT simultaneously with sub-mm ^{18}F -PET (Goorden *et al* 2013). Note that most commercial coincidence PET scanners have resolutions in the range of 0.9–1.5 mm (Constantinescu and Mukherjee 2009, Goertzen *et al* 2012, Herrmann *et al* 2013, Nagy *et al* 2013, Spinks *et al* 2014, Walker *et al* 2014).

Simultaneous acquisition of PET and SPECT tracer distributions under identical conditions can be crucial e.g. when the physiological functions studied depend on each other or when a SPECT and PET tracer have to be compared 1 : 1. It results in perfectly aligned images that enable to correlate different (patho-)physiological effects in space and time. Therefore, VECTor enables several new imaging protocols with great potential for e.g. cardiovascular, brain and cancer research (Goorden *et al* 2013). In addition, VECTor is suited for high-resolution imaging of high-energy SPECT isotopes such as ^{131}I and ^{213}Bi (de Swart *et al* 2016, van der Have *et al* 2015).

VECTor uses a clustered pinhole collimator (figure 1) to reduce strong pinhole edge penetration of 511 keV annihilation photons (Goorden and Beekman 2010, Beekman 2011). These clusters of pinholes with small opening-angles allow reducing resolution degradation due to edge penetration without sacrificing field-of-view (FOV). In VECTor, the clustered pinhole collimator is placed into a set-up with three stationary large-area gamma detectors applying continuous NaI(Tl) scintillators.

A key ingredient to obtaining high-resolution images with complex pinhole geometries is the use of statistical iterative reconstruction algorithms (Hutton *et al* 1997, Leahy and Byrne 2000, Leahy and Qi 2000, Beekman *et al* 2002, Qi and Leahy 2006). Ideally, these algorithms are based on an accurate knowledge of point spread functions (PSFs, the detector's response to a point source). All position dependent PSFs together form the system matrix, which represents the probability that a gamma photon emitted from a certain image voxel is detected in a specific detector pixel.

Several methods for obtaining PSFs for SPECT pinhole geometries are in use. A first approach is to calculate the PSFs using analytical models or computer simulations (Smith and Jaszczak 1998, Gieles *et al* 2002, Metzler *et al* 2002). In this case, several parameters that characterize the geometry of the system have to be predetermined using a calibration measurement (Li *et al* 1993, Rizo *et al* 1994, Weber *et al* 1994, Noo *et al* 2000, Beque *et al* 2003, 2005, Metzler *et al* 2005, Metzler and Jaszczak 2006, Defrise *et al* 2008). Such a calibration to obtain precise information on the geometry is important for pinhole geometries because these types of collimators make the detector's response very sensitive to small variations in parameters. This method of calculating PSFs based on some geometrical information has

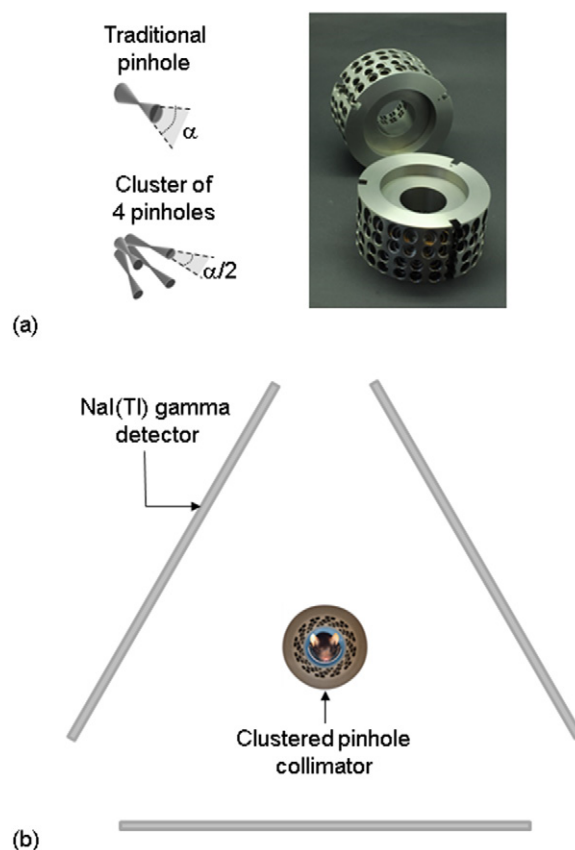


Figure 1. (a) Clustered multi-pinhole collimator for imaging gamma photons with energies from 20 to 600 keV. (b) Collimator is placed in a triangular set-up with PMT-based large-area NaI(Tl) detectors.

often been applied to SPECT systems with rotating pinholes. For stationary systems, it is in principle also feasible to directly measure the PSFs by recording the system's response to a small radioactive source that is moved sequentially to each image voxel, as was first proposed by researchers from U. of Arizona (Liu *et al* 2002, Furenlid *et al* 2004, Chen 2005, Hesterman *et al* 2007). However, the dramatically improved resolution of recently introduced small animal SPECT systems requires the use of a huge number of tiny image voxels making such measurements prohibitively long. The way to then obtain the matrix is to perform point source measurements at a limited number of voxel locations followed by model-based interpolation in order to generalize a small number of PSF properties over the whole reconstruction volume (van der Have *et al* 2008, Miller *et al* 2012). The latter approach has been in use for reconstructing U-SPECT images (Beekman *et al* 2005, van der Have *et al* 2009) on which VECTOR is based. It has resulted in both high-resolution (recently even down to 0.25 mm (Ivashchenko *et al* 2015)) and highly quantitative SPECT (Wu *et al* 2011). This method is also used to reconstruct the SPECT part of the images obtained with VECTOR.

As PSFs are energy dependent, it is not feasible to use the same system matrix for accurately reconstructing SPECT and PET images. Acquiring a PET system matrix with the same approach as used for SPECT would require manufacturing a tiny positron emitting point source (below the size of a voxel). This is challenging given the high activity concentration

that is needed to acquire a sufficient number of counts in a reasonable time, certainly, if one takes into account the relatively short half-lives of intense positron emitters. Therefore, we choose to only use the already existing set of $^{99\text{m}}\text{Tc}$ point source measurements. This not only has the advantage that no extra calibration measurement is required, but such a method can also be portable to e.g. high-energy SPECT tracers. After extracting geometrical information from $^{99\text{m}}\text{Tc}$ point source measurements one could calculate PSFs using a numerical code that incorporates similar physical effects as usually taken into account in pinhole SPECT (Goorden *et al* 2011). However, the incorporation of physical effects that are important for high-energy gamma photon transport but are not prominent at the typical energies of gamma photons emitted by SPECT tracers could possibly lead to more accurate images. Therefore the aim of this paper is twofold. We first devise a method to obtain a PET system matrix from an existing set of $^{99\text{m}}\text{Tc}$ point source measurements. Secondly, we investigate if reconstructed phantom and animal images can be improved by modelling (i) variable depth-of-interaction (DOI) in the NaI(Tl) scintillator, (ii) gamma photons traversing multiple pinholes and (iii) long tails of the PSFs for 511 keV gamma photons.

2. Materials and methods

2.1. System geometry

The mouse VECTor collimator contains 162 clustered pinholes. This collimator was integrated in a U-SPECT-II/CT system ((van der Have *et al* 2009), MILabs B.V. Utrecht, The Netherlands) that applies a triangular detector set-up with three PMT-based large-area NaI(Tl) gamma detectors. The clustered pinhole collimator applies a focusing geometry; all pinholes focus on a central scan volume. Such a design allows high count yields when imaging a specific organ or tumour (Branderhorst *et al* 2011) while larger regions up to whole body scans are done by stepping the animal through the scanner (Vastenhouw and Beekman 2007). In this paper a spiral bed sequence was used for data acquisition as it provides superior angular sampling compared to planar sequences (Vaissier *et al* 2012). More details on collimator and scanner design can be found in (Goorden *et al* 2013).

2.2. Ray tracing code for calculation of system matrix

The system matrix is pre-calculated and stored on disk. The in-house ray tracing code developed for this purpose takes into account gamma photon attenuation in the collimator and detector crystal but it ignores scatter. Inputs to the code are the pinhole positions, their axial directions, opening angles and diameters as well as the detector positions and orientations. The calibration procedure used to obtain this geometrical information is described in section 2.3 below. In our code, all pinholes are modelled as 2 overlapping cones of air intersecting the cylindrical collimator tube.

Storing system matrix elements for all possible voxel-detector pixel combinations on disk is not practical because of the large number of detector pixels (about 5×10^5 in our case) and voxels (e.g. about 2×10^6 for 0.4 mm voxel size) resulting in 10^{12} matrix elements representing a high-resolution system such as VECTor. Such a full representation of the system matrix is not necessary since for multi-pinhole geometries these matrices are quite sparse; only gamma photons that go through the pinholes or that pass the pinholes close to the hole's edge have a considerable probability to pass through the collimator and be detected. Therefore, we implemented a cut-off C in our code with a value in between 0 and 100%. When a certain value of C is set, only those gamma photon paths that have a probability $>C$ to pass through the collimator material are incorporated into the system matrix.

2.2.1. Calculation of path length through the collimator material. The ray tracing code calculates the path length through the collimator material ΔL_{ij} encountered by a photon traveling from image voxel i to detector pixel j . This calculation is done analytically. For such a calculation, the intersection point of the gamma photon path with the inner collimator wall, the outer collimator wall and with each of the pinholes it encounters is determined. Since the cylindrical collimator and the pinhole cones can be described by quadratic equations and the gamma photon path by a linear equation, calculating these intersection points amounts to solving a quadratic equation. Note that we explicitly include the possibility that a gamma photon path intersects with multiple pinholes. We therefore calculate intersection points of a gamma photon with multiple pinholes instead of determining the response of single pinholes to a point source. Assuming that the collimator material is characterized by a linear attenuation coefficient μ_{coll} , the collimator attenuation is then given by $\exp(-\mu_{\text{coll}}\Delta L_{ij})$. If this attenuation exceeds the pre-set cut-off C , detector pixel j is set to a value of

$$P_{ij}^{\text{coll}} = W_{ij} \exp(-\mu_{\text{coll}}\Delta L_{ij}) \quad (1)$$

Here W_{ij} is a geometric factor presenting the probability that a gamma photon emitted from voxel i would be detected in detector pixel j in the absence of a collimator (it depends on the solid angle).

2.2.2. Detector blurring. After the detector image for one particular point source position is calculated this way, non-idealities of the detector are incorporated. We model variable DOI by convolving the detector image with a position-dependent kernel P^{det} resulting in a DOI-corrected image P^{DOI} ;

$$P_{ij}^{\text{DOI}} = \sum_k P_{ik}^{\text{coll}} P_{kj}^{\text{det}(i)}. \quad (2)$$

Here $P_{kj}^{\text{det}(i)}$ represents the probability that a gamma photon emitted from voxel i and entering the detector in pixel k is detected in pixel j . It is calculated using Beer's law;

$$P_{kj}^{\text{det}(i)} = \int_{l_1^{ijk}}^{l_2^{ijk}} dl \exp(-\mu_{\text{det}} l) \mu_{\text{det}} = \exp(-\mu_{\text{det}} l_1^{ijk}) - \exp(-\mu_{\text{det}} l_2^{ijk}) \quad (3)$$

Here μ_{det} is the linear attenuation coefficient of the NaI(Tl) scintillator at the gamma photon's energy, l_1^{ijk} and l_2^{ijk} are distances travelled through the scintillator until the gamma photon enters or leaves pixel j respectively (see figure 2(a)). Note that this way we do not only model a shift in detected position due to variable DOI, but also the resulting shape distortion of PSFs. Subsequently, to model additional detector non-idealities, Gaussian detector blurring with a FWHM of 3.5 mm is applied to the detector image (the intrinsic resolution of the gamma detector).

DOI modelling can be turned on and off. If variable DOI is modelled for 511 keV gamma photons, the raytracer traces the gamma photon through the scintillator as described by equations (2) and (3) and thus DOI is automatically included in the system matrix. If DOI modelling is off, it is assumed that the gamma photon is detected in the pixel in which it enters the gamma detector (effectively, the attenuation coefficient in equation (3) is set to infinity).

2.3. Calibration procedure

We use results of the SPECT calibration procedure with a scanning $^{99\text{m}}\text{Tc}$ point source described in van der Have *et al* (2008). In this procedure, the PSF location on the detector

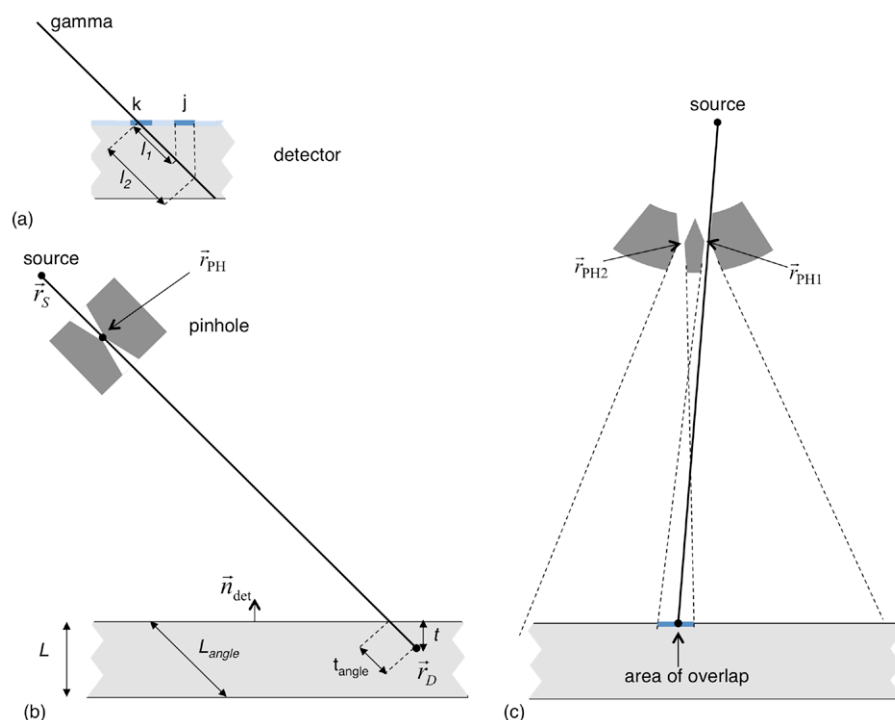


Figure 2. (a) Gamma entering the detector under an angle in pixel k is assumed to be detected in pixel j if it travels a distance $>l_1$ and $<l_2$ in the detector crystal. (b) Model used for fitting collimator location, collimator orientation, detector location and detector orientation to the point source calibration measurement. It is assumed that source location \vec{r}_S , pinhole center \vec{r}_{PH} and detection point \vec{r}_D lie on a straight line. (c) Pinhole projections in VECTor slightly overlap on the detector as is illustrated here. When a PSF is measured in this area of overlap, a line is drawn from source position to PSF location and distance from this line to pinhole centres (\vec{r}_{PH1} and \vec{r}_{PH2} in this case) is determined. As in this example the line is closest to \vec{r}_{PH1} , pinhole 1 is assumed to be corresponding to this PSF.

and the corresponding pinhole are determined for each measured point source projection. Compared to the description in van der Have *et al* (2008) we made one small adaptation; in contrast to common U-SPECT collimators, the VECTor collimator results in slightly overlapping pinhole projections. When the PSF is measured in such an overlapping area, we determine the corresponding pinhole by drawing a line between point source and PSF location and calculating to which pinhole's centre it is closest as is illustrated in figure 2(c). As we have only slight overlap as illustrated in the figure, there is no ambiguity in pinhole choice. For the VECTor collimator, the ^{99m}Tc point source is measured in 676 point source locations leading to 25 263 projections on the detector (as the point source projects through multiple pinholes).

PSF locations are then used to determine a number of geometrical parameters describing VECTor's geometry. For the geometry, we assume that the relative pinhole placement in the collimator tube, the pinholes' diameters and opening angles are as designed. However, we allow the whole cylindrical collimator tube as well as the 3 gamma detectors to be shifted and rotated with respect to the design. Generally, a translation and rotation of a rigid body can be parameterized by 6 parameters (3 rotation angles and a 3D translation). Therefore, we have

24 free parameters (6 for the collimator and 6 for each of the 3 detectors) to be fitted. Note that with the 25 263 point source projections that were measured this fit is strongly overdetermined. However, as this point source data was recorded anyway for determining the SPECT matrix, we did not try to reduce the number of point source locations although we believe that this would certainly be possible.

The mathematical model that we use for fitting assumes that the position of the point of detection, the pinhole centre and the source are on the same line (an approximation validated for SPECT image reconstruction (van der Have *et al* 2008)). Furthermore, it assumes that the point of detection lies below the detector surface at the average DOI in the scintillation crystal (see figure 2(b)).

Collimator rotation and translation with respect to the design are described by a standard rotation matrix M_{coll} (can be expressed using 3 Euler angles) and a translation vector \vec{r}_{coll} . Thus, if a certain pinhole is designed to be at position \vec{r}_{PH0} , its fitted position is at

$$\vec{r}_{\text{PH}} = M_{\text{coll}} \cdot \vec{r}_{\text{PH0}} + \vec{r}_{\text{coll}}. \quad (4)$$

For detector n ($n = 1 \dots 3$), we assume a local coordinate system (X, Y) on the detector plane. A point that lies at a distance t below the detector plane is then expressed in the 3D coordinate system as

$$\vec{r}_D = M_{\text{det}, n} \cdot \begin{pmatrix} X \\ Y \\ -t \end{pmatrix} + \vec{r}_{\text{det}, n}. \quad (5)$$

Here $M_{\text{det}, n}$ and $\vec{r}_{\text{det}, n}$ are rotation matrix and translation vector characterizing the n th detector. Assuming that the gamma photon travels from source position \vec{r}_S through the pinhole centre \vec{r}_{PH} to the detector means that the unit vector describing its travel direction is

$$\vec{v}_\gamma = \frac{(\vec{r}_{\text{PH}} - \vec{r}_S)}{\|\vec{r}_{\text{PH}} - \vec{r}_S\|}. \quad (6)$$

Here $\|\dots\|$ denotes the magnitude of the vector. With these definitions, we can build our mathematical model.

We now express the average DOI t into equations. The gamma photon entering the detector under an angle can maximally travel a distance L_{angle} in the detector crystal (see figure 2(b)). This distance relates to the detector thickness L via the relationship $L_{\text{angle}} = L / |\vec{v}_\gamma \cdot \vec{n}_{\text{det}, n}|$ where \cdot denotes the inner product and $\vec{n}_{\text{det}, n}$ is the unit vector perpendicular to the n 'th detector. Of all gamma photons that have an interaction in the scintillator, the average distance they will have travelled in the scintillator reads

$$\begin{aligned} t_{\text{angle}} &= \frac{\int_0^{L_{\text{angle}}} dx \mu_{\text{det}} \exp(-\mu_{\text{det}} x) x}{\int_0^{L_{\text{angle}}} dx \mu_{\text{det}} \exp(-\mu_{\text{det}} x)} \\ &= \frac{1 - \exp(-\mu_{\text{det}} L_{\text{angle}})(1 + \mu_{\text{det}} L_{\text{angle}})}{(1 - \exp(-\mu_{\text{det}} L_{\text{angle}}))\mu_{\text{det}}} \end{aligned} \quad (7)$$

and $t = t_{\text{angle}} |\vec{n}_{\text{det}, n} \cdot \vec{v}_\gamma|$.

Assuming that the detection point \vec{r}_D lies on the same line as the pinhole position and source position means that $\vec{r}_D = c \cdot \vec{v}_\gamma + \vec{r}_S$ with c a constant yet to be determined. Using equation (5) we can then write

$$c \cdot \vec{v}_\gamma + \vec{r}_S = M_{\text{det},n} \cdot \begin{pmatrix} X \\ Y \\ -t \end{pmatrix} + \vec{r}_{\text{det},n} \quad (8)$$

Equation (8) is a set of 3 linear equations in which the available data (X and Y of each point source projecting on the detector) is expressed in terms of the parameters that have to be estimated ($M_{\text{det},n}$, $\vec{r}_{\text{det},n}$ for $n = 1 \dots 3$, M_{coll} and \vec{r}_{coll}) and a set of known parameters (\vec{r}_{PH0} , \vec{r}_S , L and μ_{det}). This is the desired form for parameter estimation by fitting.

Fitting was performed using the Levenberg–Marquardt algorithm. To assess how well the measured PSF locations corresponded to the locations estimated from the pinhole-detector geometry, we recorded the average distance between the measured and estimated locations. Prior to the fit when we assumed that the collimator-detector geometry was as designed, we found that the average distance was 8.8 mm. We then performed a first 24 parameter fit with all 25 263 data points (PSF locations). After this fit the average error had reduced to 0.79 mm with a maximum error of 8.5 mm. We then removed all outliers, i.e. data points with error larger than 2 mm. This led to a removal of 1340 out of 25 263 data points. We then performed a second fit without outliers. After this fit was finished, the average error (of remaining data points) was reduced to 0.68 mm with a maximum error of 2.9 mm. In supplemental figure 7 we show how this error between measured and estimated PSF locations varies over the detector area. From this figure it is clear that the largest errors were made near the detector edges which we believe may be due to the fact that variable DOI has the largest influence there (as angle of incidence is largest, see figure 1(b)).

2.4. Positron range

We take into account the finite positron range by pre-calculating the probability that a positron emitted in voxel i annihilates in another voxel j . These probabilities are calculated using Geant4 (Agostinelli *et al* 2003, Allison *et al* 2006). An isotropic point source of the specific positron-emitting nuclide is simulated in water and 10^6 events are simulated. The annihilation position of the emitted positron from the Geant simulation is binned into voxels of the same size as the reconstruction grid. To reduce noise, a spherically symmetric averaging is applied such that voxel locations at the same distance from the positron emitter location will have the same value. The resulting volume is stored and used as a 3D convolution kernel during reconstruction.

In principle, positron ranges could be incorporated directly into the system matrix. However, since such an inclusion would significantly increase the computational burden, we incorporate positron range in the forward projection of our reconstruction algorithm only (see next section).

2.5. Image reconstruction

We used pixel-based ordered subsets expectation maximization (POSEM, (Hudson and Larkin 1994, Branderhorst *et al* 2010)) with 32 subsets. For phantom scans, images obtained after different iteration numbers are shown and compared. The positron range was included in the forward projection (which effectively results in a dual-matrix approach (Zeng and Gullberg 1992, Kamphuis *et al* 1998)). Scatter correction was performed using a triple energy window correction (King *et al* 1997) with side windows adjacent to the photo peak. Energy window setting for all experiments are provided in table 1. The difference between energy window settings for different imaging studies is due to the fact that the 511 keV photopeak was slightly shifting over time. In all studies, the photopeak window was centered around the maximum

Table 1. Energy window settings for different reconstructions and number of counts measured.

Scan	Photopeak window	Background windows	Counts in photopeak window	Counts in background windows
Hot-rod Derenzo phantom I	435–531 keV	355–435 keV 531–611 keV	$375 \cdot 10^6$	$86.9 \cdot 10^6$
Uniformly filled syringe	435–531 keV	355–435 keV 531–611 keV	$89.8 \cdot 10^6$	$27.2 \cdot 10^6$
Mouse cardiac	448–548 keV	368–448 keV 548–628 keV	$18.2 \cdot 10^6$	$5.63 \cdot 10^6$
Whole body mouse bone	430–526 keV	350–430 keV 526–606 keV	$25.3 \cdot 10^6$	$7.63 \cdot 10^6$
Focused mouse bone	462–564 keV	382–462 keV 564–644 keV	$21.9 \cdot 10^6$	$5.87 \cdot 10^6$
Hot-rod Derenzo phantom II	435–531 keV	355–435 keV 531–611 keV	$246 \cdot 10^6$	$55.6 \cdot 10^6$

in the measured energy spectrum and had a width of 20% of its central value. As different matrices model different effects the reconstructed images contain quite different absolute values of reconstructed activities. To be able to scale all images to the same colormap scale, we determined a calibration coefficient for each system matrix used. The calibration coefficient was determined by calculating the reconstructed activity inside the uniformly filled syringe imaged in this paper (see section 2.8.3). To this end, a cylindrical region-of-interest of 10 mm diameter inside the syringe was used.

2.6. Fixed parameters

We assumed fixed pinhole diameters of 0.76 mm and pinhole opening angles of 16° (outer rings) or 18° (inner ring) conforming to the design. An attenuation coefficient $\mu_{\text{coll}} = 0.23 \text{ mm}^{-1}$ was assumed corresponding to a collimator material composition of 97% Tungsten (18.5 g cm^{-3} density), 1.5% iron and 1.5% nickel. For the detector we assumed $\mu_{\text{det}} = 0.21 \text{ mm}^{-1}$ for 140 keV gamma photons (needed for calibration) and $\mu_{\text{det}} = 0.012 \text{ mm}^{-1}$ for 511 keV. These detector attenuation coefficients were determined by Monte Carlo simulations using Geant4. In these simulations, we recorded energy loss of the gamma photon in the 9.0 mm thick NaI crystal by photoelectric effect and Compton scattering (gamma photon incidence was perpendicular). The total energy loss of each gamma photon was summed. The finite detector energy resolution was then mimicked by randomly generating the measured energy from a Gaussian probability distribution centered around the total summed energy and with 10% FWHM. This way, the fraction f of gamma photons entering the detector that would be detected within the photopeak window (having a width of 20% as in the experiments) was estimated. A detector attenuation coefficient that would lead to that detector efficiency according to Beer's law, i.e. $\exp(-\mu_{\text{det}} \cdot 9 \text{ mm}) = f$, was then determined. This way, μ_{det} includes the photoelectric effect and the part of the Compton scatter that ends up being detected in the photo peak.

2.7. Analysis of the effect of different tail cut off C and MPP on system matrices

In this paper we analyze the effect on reconstructed images of (1) including variable DOI in the gamma detector, (2) incorporating multiple pinhole paths (MPP) and (3) different levels of tail

cut off C . To get a better understanding of the effect of varying C , we first generated a series of matrices on a rough voxel grid of 1.6 mm for a wide range of C values from 0.01%–20%. For each value of C , two matrices were generated, one including MPP and one without MPP incorporated. We chose a rough voxel grid because this allowed us to also test very low C values (i.e. $C = 0.01\%$, meaning that all gamma photon paths with a probability $>0.01\%$ of passing through the collimator were modelled). As such low C values lead to matrices with many elements, these are hard to generate on finer voxel grids. It can be expected that these gamma photon paths with small probabilities of occurring only affect reconstructed images if the photon flux carried by them is significant. To get an idea of this flux, we summed all matrix elements in each of the generated system matrices. This provides a measure of the modelled flux averaged over the FOV. These flux values were then normalized to the flux obtained with the matrix with the lowest cut off ($C = 0.01\%$) and with MPP included. In this first analysis of system matrices, we did not include DOI as this does not affect the percentage of the total flux that is modelled.

2.8. Phantom studies

Different phantom studies were performed and analyzed to quantitatively assess reconstructions with different system matrices. For each of the experiments, the total number of counts in photopeak and background windows (used for scatter correction, see section 2.5) is provided in table 1.

2.8.1. Hot-rod derenzo phantom. A hot-rod Derenzo resolution phantom was filled with a 54 MBq ^{18}F solution and scanned for 4 h. The phantom had 6 sectors each containing a set of equally sized capillaries with diameters of 0.7, 0.8, 0.9, 1.0, 1.2 and 1.5 mm. The distance between capillary centres was equal to twice the capillary diameter. For visualization a 0.5 mm FWHM 3D Gaussian filter was applied to reconstructed images.

On (unfiltered) phantom reconstructions, a contrast-noise analysis similar to the one presented in (Walker *et al* 2014) was done. The images were resampled to a fine grid and ROIs with a diameter of 0.9 times the rods sizes were then placed on and in-between the rods (supplemental figure 1 (stacks.iop.org/PMB/61/3712/mmedia)). ROI placement was repeated on subsequent 0.4 mm thick slices for a total number of 10 planes. In each of the ROIs, the activity was determined. Define h_{ijk} to be the activity in a ROI placed in sector i on rod j in slice k . Similarly, the activity in each of the ROIs in between rods can be denoted by c_{ijk} . For a certain sector i , let \bar{h}_i be the mean activity in all ROIs placed on top of the rods in all slices and let \bar{c}_i be the mean activity in the ROIs placed in between. We then define the contrast in that sector as $C_{\text{rods},i} = \frac{\bar{h}_i - \bar{c}_i}{\bar{h}_i}$.

Furthermore, to represent variability in ROI mean values we calculated for each sector i the standard deviation $\sigma_{h,i}$ and $\sigma_{c,i}$ of h_{ijk} and c_{ijk} respectively over all ROI positions and over all slices. The noise in sector i is then calculated as $N_{\text{rods},i} = \sqrt{\sigma_{h,i}^2 + \sigma_{c,i}^2} / (\bar{h}_i + \bar{c}_i)$.

2.8.2. Hot-rod derenzo phantom II. A second hot-rod Derenzo phantom was filled with a 57 MBq ^{18}F solution and scanned for 1 h. This phantom had smaller capillaries and could therefore be used to test if resolution was improved by the use of new reconstruction software. Capillaries had diameters of 0.45, 0.5, 0.55, 0.75, 0.8 and 0.85 mm. For visualization, a 0.4 mm FWHM 3D Gaussian filter was applied.

2.8.3. Uniformly filled syringe. A 12 ml syringe (15.9 mm inner diameter, 6 cm length) was filled with 65 MBq ^{18}F solution and scanned for 3.5 h. As will be apparent from the results, in some cases part of the activity was reconstructed outside the syringe. To quantify this, activity in a cylindrical annulus with 19 mm inner radius and 25 mm outer diameter around the phantom was determined (supplemental figure 1). Activity reconstructed in this cylindrical annulus outside the phantom was reported as a percentage of total reconstructed activity (for unfiltered images). For visualization, images were filtered with a 0.8 mm FWHM 3D Gaussian.

2.9. Animal studies

Animal studies were carried out in accordance with the Dutch Law on Animal Experimentation and conducted according to protocols approved by the Animal Research Committee of the University Medical Center Utrecht. For each animal scan, the total number of counts is provided in table 1.

2.9.1. Mouse cardiac scan. A 29 g C57Bl6 mouse was anesthetized with isoflurane and subsequently injected intravenously with 24 MBq ^{18}F -deoxyglucose (^{18}F -FDG) and 130 MBq $^{99\text{m}}\text{Tc}$ -tetrofosmin (not shown here). A 60 min acquisition began 10 min post injection. Images were reconstructed using 15 iterations. For visualization, images were post-filtered with a 0.8 mm FWHM 3D Gaussian.

2.9.2. Mouse bone scans. A 33 g C57Bl6 mouse was anesthetized with isoflurane and injected intravenously with 49 MBq ^{18}F -fluoride and 141 MBq $^{99\text{m}}\text{Tc}$ -MDP (not shown here). A 60 min whole-body acquisition was performed, starting 30 min post injection. Images were reconstructed using 15 iterations and post-filtered with a 0.8 mm FWHM 3D Gaussian. A 27 g C57Bl6 mouse was anesthetized with isoflurane and injected intravenously with 85 MBq ^{18}F -fluoride and 130 MBq $^{99\text{m}}\text{Tc}$ -HDP (not shown here). A 15 min acquisition of the lumbar spine and the pelvis was performed, beginning 60 min post injection. For reconstruction, 30 iterations were used. A 0.4 mm FWHM 3D Gaussian post-filter was applied.

3. Results

3.1. Analysis of system matrices

Relative flux modelled into the system matrices as function of tail cut off C is shown in figure 3, both for system matrices with and without MPP. If one sets a tail cut off $C = 20\%$ (a value we initially chose as it is more than sufficient for reconstructions of SPECT images (van der Have *et al* 2008)), only 35% of the flux is modelled. For such a value of the tail cut off, including MPP does not have an effect; apparently only gamma photon paths close to the pinhole's edge are incorporated into the matrix and these paths do not pass through multiple pinholes (for $C = 20\%$ and $C = 10\%$ matrices with and without MPP are exactly identical). For lower tail cut offs, MPP start to play a role. For $C = 5\%$, 48% and 47% of the flux is modelled with or without MPP included respectively. These numbers increase to 70% and 65% for $C = 1\%$, 79% and 72% for $C = 0.5\%$ and 93% and 82% for $C = 0.1\%$.

As a reference, we plotted a similar curve for a SPECT matrix (140 keV) made with the same ray tracing software as used for 511 keV system matrices. For this lower energy, we found that incorporating MPP does not have any effect, thus only 1 curve is plotted. Clearly, for 140 keV the PSF tails carry much less weight than for 511 keV; for $C = 20\%$, 83% of the flux is already modelled while for $C = 1\%$, 99% is taken into account.

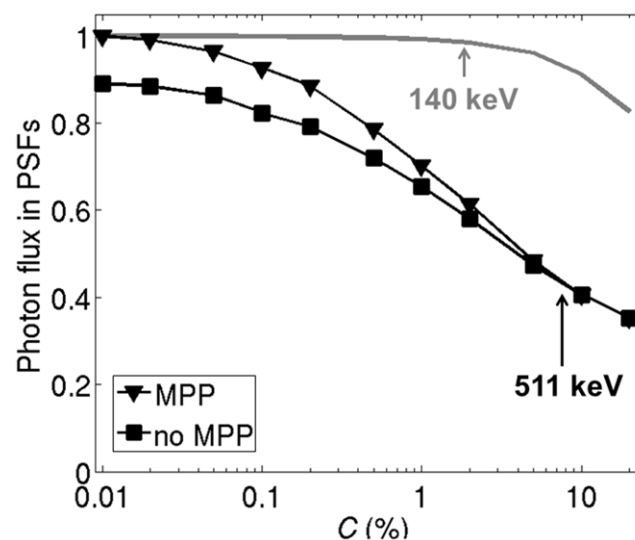


Figure 3. Gamma photon flux modelled in 511 keV system matrices as a function of tail cut off level C . Results are shown for matrices with and without MPP incorporated. As a reference a curve for 140 keV (typical energy of SPECT tracers) was also shown. In the latter case, curves with and without MPP fall on top of each other. Plotted flux values are relative to the flux obtained for $C = 0.01\%$ with MPP included.

These results suggest that for reconstructing PET tracer distributions on VECTor, it may be beneficial to use much lower tail cut offs than is commonly used in SPECT. However, as C is lowered the number of system matrix elements rapidly increases; compared to a system matrix with $C = 20\%$, matrices with $C = 5\%$, $C = 1\%$, $C = 0.5\%$ and $C = 0.1\%$ have a factor of 3.2, 18, 34 and 116 more matrix elements, respectively. Thus, computational load of image reconstruction rapidly grows as one tries to incorporate a larger part of the flux. Therefore, in this paper we only show reconstructed images for $C = 0.5\%$ and higher. In the discussion section we return to this issue and we suggest possible future schemes for acceleration.

3.2. Hot-rod derenzo phantom I

In figure 4 reconstructed images of the first hot-rod Derenzo phantom are shown. The 4 panels represent different physical effects that were included into the reconstruction. In figures 4(a) and (b) variable DOI in the gamma detector was not modelled while it was taken into account in the bottom panels (figures 4(c) and (d)). MPP were only included in the right panels (figures 4(b) and (d)). Reconstructions with tail cut offs C of 20%, 5%, 1% and 0.5% are shown after 15, 30 and 60 iterations. Visually, using $C = 0.5\%$ or $C = 1\%$ resulted in much less noisy reconstructions and clearer rod visibility than when $C = 20\%$ was used. By visually comparing different panels of figure 4 it can be seen that including a model for variable DOI has a distinct effect as well; if DOI modelling is not included, rods have a somewhat triangular appearance while reconstructed images incorporating variable DOI (figures 4(c) and (d)) result in circular rods which conforms to reality. Finally, including gamma photons paths traversing multiple pinholes does not have a clear visible effect on reconstructed images.

In figure 5 contrast-over-noise ratio (CNR) as a function of iteration number is shown for the 1.0 mm rod diameter sector of the same hot-rod Derenzo phantom as in figure 4. Panels 5a–5d correspond to panels 4a–4d with respect to physical effects that were included in image

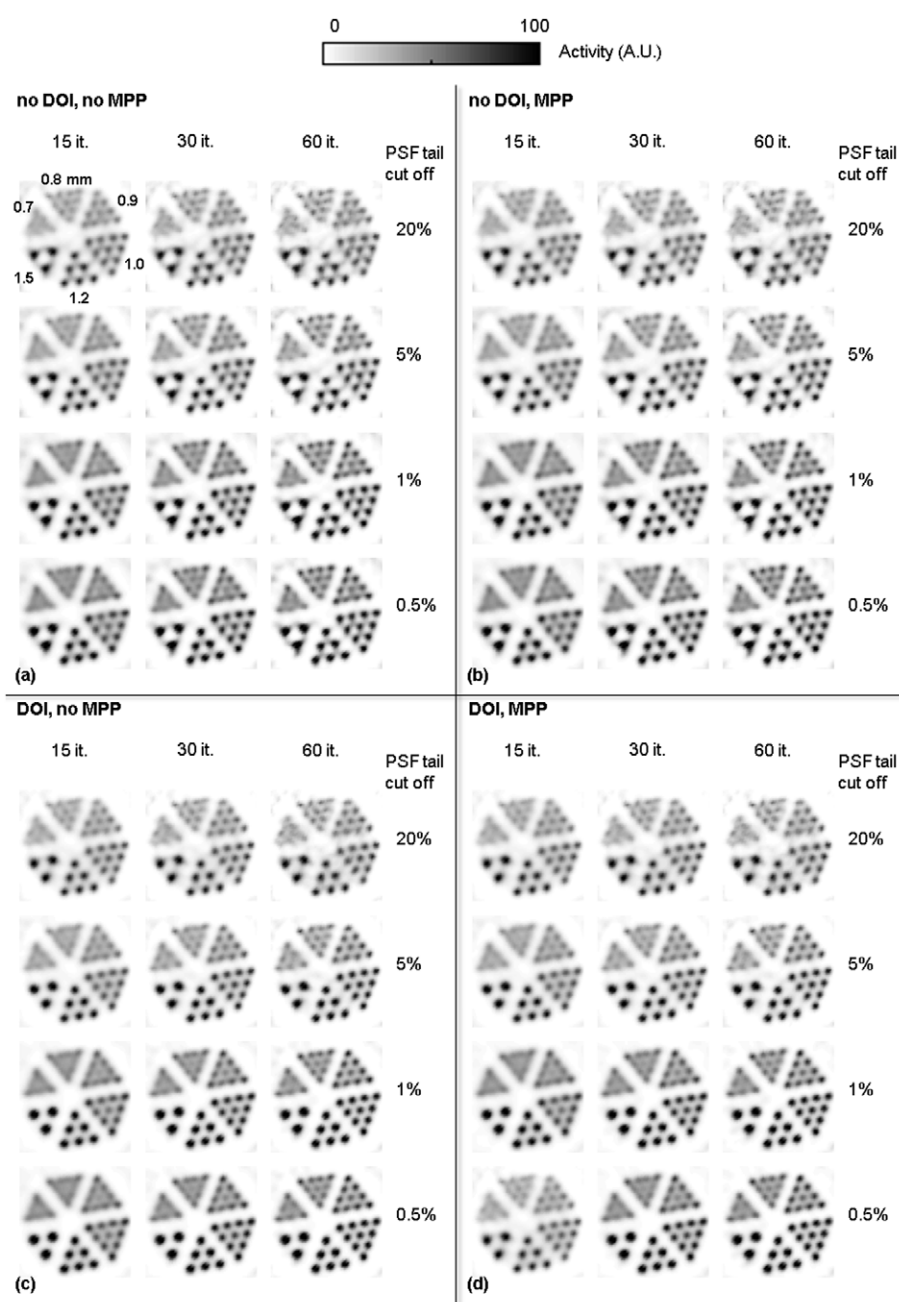


Figure 4. Reconstructed images of hot-rod Derenzo phantom I. System matrices on which reconstructions were based contained different physical effects; varying DOI in the scintillator was not taken into account in (a) and (b) but was modeled in (c) and (d) while multiple-pinhole paths (MPP) were only accounted for in (b) and (d). Reconstructions after 15, 30 and 60 iterations are shown for different tail cut offs (20%, 5%, 1%, and 0.5%).

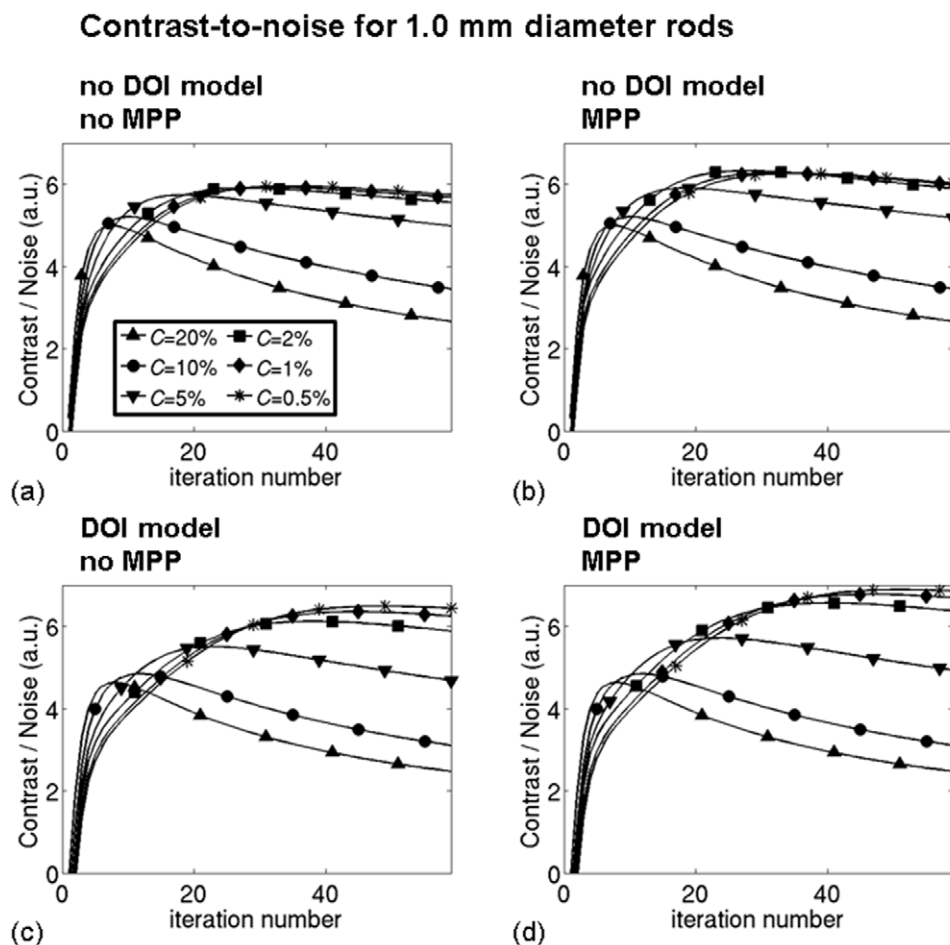


Figure 5. CNR ratio for 1.0 mm rods in the hot-rod Derenzo phantom I versus iteration number. System matrices on which reconstructions were based contained different physical effects; varying DOI in the scintillator was not taken into account in (a) and (b) but was modeled in (c) and (d) while multiple-pinhole paths (MPP) were only accounted for in (b) and (d). Different symbols correspond to different levels of tail cut off C .

reconstruction. Different symbols correspond to different values of C . Note that in this graph we also show results for tail cut off values $C = 10\%$ and $C = 2\%$ which were not shown in figure 4 due to paper length considerations. These CNR curves confirm the earlier visual assessment; for each of the panels a lower C results in better CNR characteristics. It can also be seen that for small C larger numbers of iterations are needed to reach optimal CNR. On average (over the 4 panels of figure 5) optimal CNR improved by 4.4%, 19%, 30%, 32% and 33% when C was lowered from 20% to 10%, 5%, 2%, 1% and 0.5% respectively. Remarkably, lowering the tail cut off from 20% to 10% has a relatively small effect on CNR, while further decreases to 5% and 2% both have a large impact. Optimal CNR for 2%, 1% and 0.5% were rather close.

In supplemental figures 2–6, CNR curves are plotted for the other sectors of the phantom. For all sectors a lower C is preferable if one wants to reach the highest CNR ratio. These curves are in general agreement with results discussed above; a decrease of C from 20% to

10% has a much lower impact on CNR than a lowering of C from 10% to 5%. Results for 2%, 1% and 0.5% are generally close.

To better compare the effect of differences in MPP and DOI modelling, figure 6 shows contrast versus noise for a single tail cut off setting $C = 1\%$ for all rod diameters. Apparently, including a DOI model and MPP always leads to best contrast at a given noise level for higher iterations (i.e. when most contrast has been recovered), although the effect of including MPP is minor and sometimes even negligible. Thus, once converged highest CNR is found when DOI and MPP are included. In earlier iterations (for lower noise levels) this is not always the case. For the larger rods, better CNR is initially obtained when DOI is not modelled. We believe that this is due to faster convergence in the case that DOI is not included as in that case PSFs are more narrow and the reconstruction problem is less ill-posed. At a certain point a crossover between CNR curves with and without DOI model occurs. A similar crossover (but less clear) can be seen for the largest two rod sectors between the curve with DOI and MPP included and the curve with DOI but no MPP included.

Note that from figure 6 it is clear that for the 0.7 mm rods more contrast may be recovered if we would increase the number of iterations. We have tried this for the matrix with 1% tail cut off that included DOI and MPP. However, we found that with more iterations 0.7 mm rods could still not be distinguished and due to simulation time considerations (as we are doing many different reconstructions in the paper), we have decided to limit ourselves to 60 iterations in our analysis.

3.3. Uniformly filled syringe

Figure 7 shows reconstructed images of a uniformly filled syringe. Two slices in mutually perpendicular directions are provided. Similar to hot-rod Derenzo phantom images shown in figure 4, the panels indicate different physical effects that were included in the system matrix. Reconstructed images with different tail cut offs C of 20%, 5%, 1% and 0.5% are shown in each of the panels after 30 iterations. For these images, the effect of incorporating long tails is most pronounced while including MPPs or DOI has a smaller visual effect. Images with lowest C resulted in the most uniform reconstructions while the amount of activity visible outside the phantom is lowest. This is confirmed by the data in table 2, which quantifies the amount of reconstructed activity outside the phantom relative to total reconstructed activity. This table shows that lowering cut off from 20% to 5% does not have a large effect on activity reconstructed outside the phantom which only starts to disappear for values of $C = 2\%$ or less. Including DOI and MPP paths both have a similar effect for this figure of merit; e.g. for $C = 0.5\%$ activity reconstructed outside the phantom is 6.9% when DOI and MPP were not included, 5.2% when only one of these effects is included and 3.8% when both effects are taken into account.

3.4. Effect of improved reconstruction software on phantom and mouse images

Based on the phantom experiments described above we chose to further compare reconstructed mouse and phantom images for 3 different system matrix models. As an ‘initial’ version of the software we set $C = 20\%$ and did not model DOI and MPP. To assess how an ‘intermediate’ level of modelling affects reconstructed images we included DOI and MPP and set $C = 5\%$. Such a tail cut off can already lead to significant improvements in CNR (as shown for the first hot-rod Derenzo phantom) but is still reasonably fast. To test a more ‘accurate’ level of modelling we also show reconstructed images for a lower tail cut off of 1% as this further improved contrast-to-noise characteristics in the hot-rod Derenzo phantom I and lead to

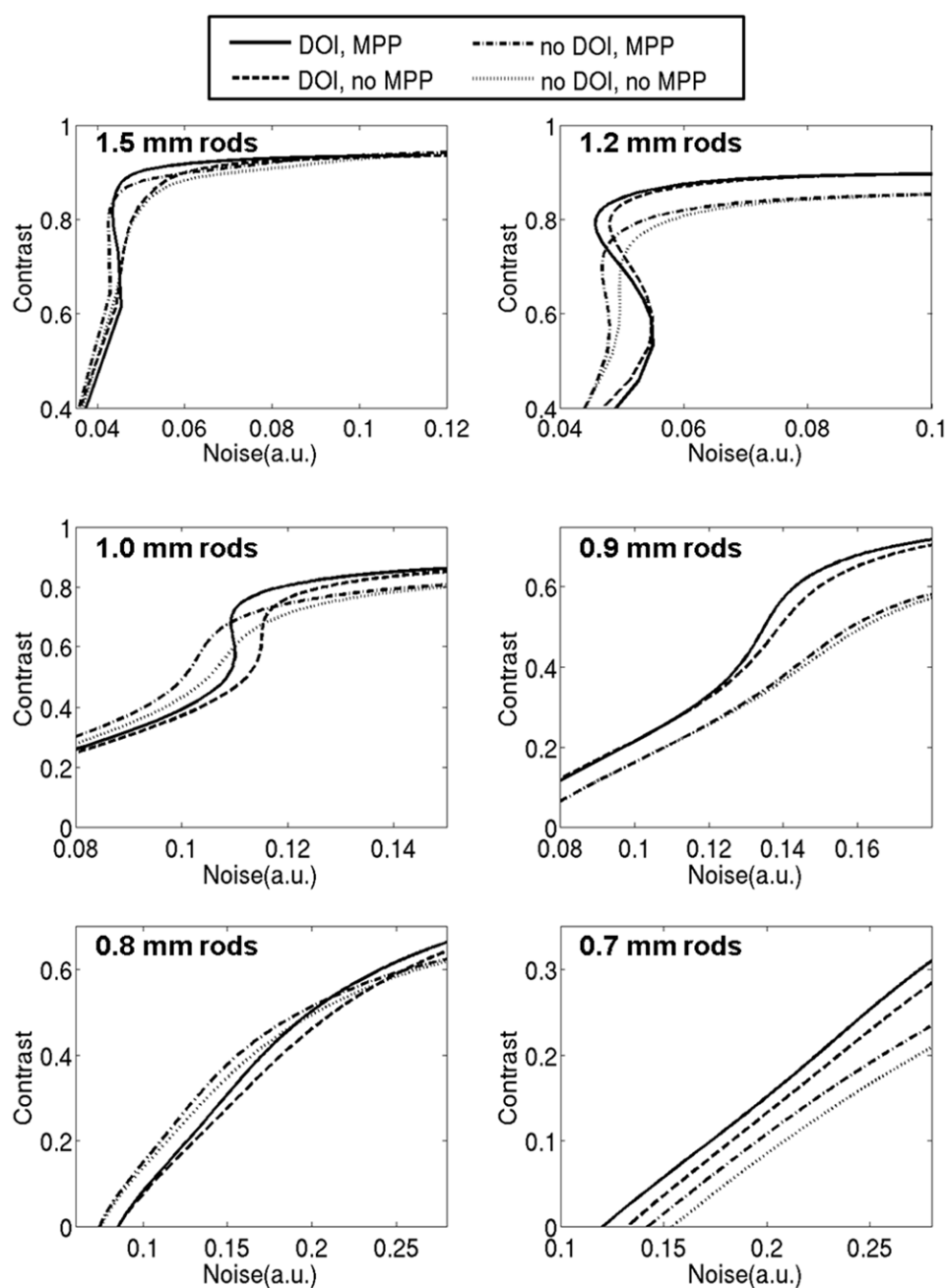


Figure 6. Contrast versus noise curves for all rod sectors in the hot-rod Derenzo phantom I. In all reconstructions, tail cut off was set at 1% while different physical effects were included.

strongly suppressed levels of background noise in the uniformly filled syringe. Lower values of C may further decrease background noise (e.g. $C = 0.5\%$ in the uniformly filled syringe) but it leads to impractical long reconstruction times with current software.

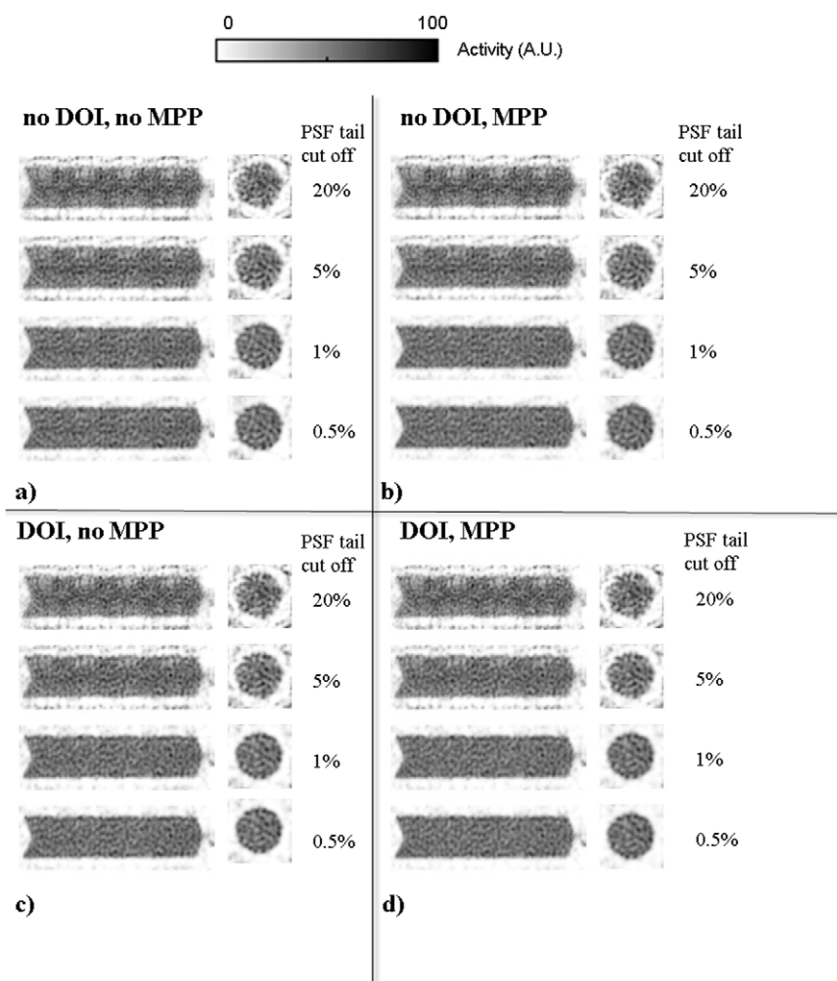
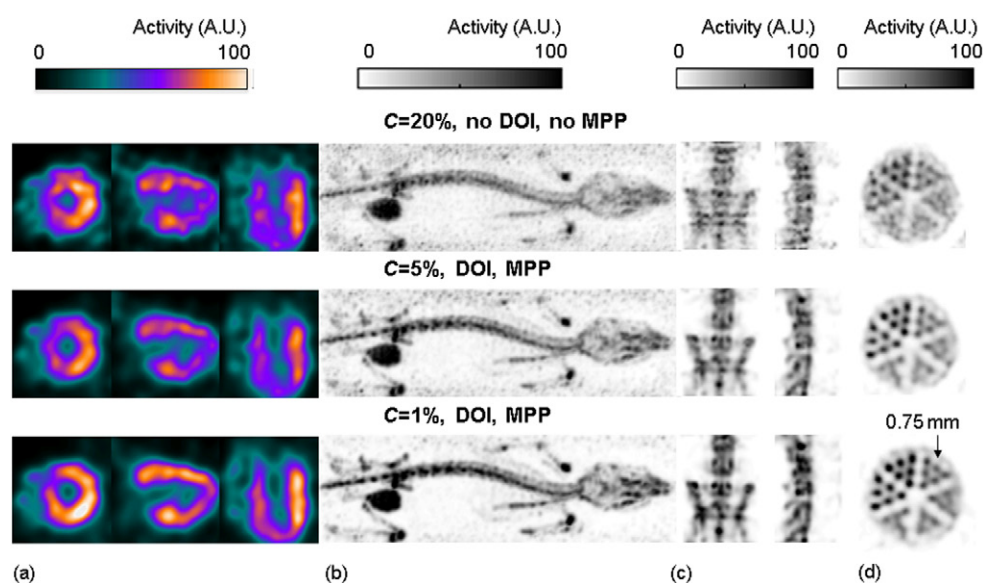


Figure 7. Reconstructed images of a uniformly filled syringe. Slices in two mutually perpendicular directions are shown. System matrices on which reconstructions were based contained different physical effects; varying DOI in the scintillator was not taken into account in (a) and (b) but was modeled in (c) and (d) while multiple-pinhole paths (MPP) were only accounted for in (b) and (d). Reconstructions obtained after 30 iterations are shown for different tail cut offs (20%, 5%, 1%, and 0.5%). Slice thickness was 3.2 mm.

As the ground truth is not known, differently reconstructed mouse scans are harder to compare than phantom images. In general, the cardiac scan and the focused and whole body bone scans shown in figure 8 appear to have lower levels of background and better resolution when DOI and MPP are included and when C is lowered. Based on a visual assessment, the difference between $C = 5\%$ and $C = 1\%$ seems most significant for the whole body mouse bone scan for which $C = 1\%$ leads to much lower background levels than $C = 5\%$. This is in agreement with phantom scan results from the uniformly filled syringe. The reconstructed hot-rod Derenzo phantom II (figure 8(d)) scan (with smaller rods than the first one shown in figure 4) shows that for $C = 1\%$ 0.75 mm rods are clearly visible.

Table 2. Reconstructed activity outside uniform phantom relative to total activity for reconstructions of figure 7.

PSF tail cut off	no DOI, no MPP	no DOI, MPP	DOI, no MPP	DOI, MPP
20%	13%	13%	12%	12%
10%	13%	13%	12%	12%
5%	12%	11%	11%	10%
2%	8.7%	7.4%	7.6%	6.2%
1%	7.5%	6.4%	6.1%	4.9%
0.5%	6.9%	5.2%	5.2%	3.8%

**Figure 8.** Effect of modelling improvements on reconstructed mouse images. Images obtained with an ‘initial’ version of reconstruction software with 20% PSF tail cut off, no DOI modelling and no MPP is compared with version with DOI modelling and MPP included for $C = 1\%$ and $C = 5\%$. (a) Three mutually perpendicular slices through the mouse’s heart. Images represent an average over the cardiac cycle. Slice thickness was 0.8 mm. (b) Maximum intensity projections of a whole body mouse bone scan. (c) Maximum intensity projections of a mouse bone scan focused on the lumbar spine and pelvis. (d) Hot-rod Derenzo phantom II with 0.85, 0.8, 0.75, 0.55, 0.5, 0.45 mm diameter rods. Image shows that with new image reconstruction 0.75 mm rods can be distinguished. Slice thickness was 4 mm.

4. Discussion

In this paper it was shown that for reconstruction of PET images on VECTor, using similar physical modelling as used for SPECT reconstruction results in far from optimal images. Images are strongly improved by taking into account effects specific to the high-energy annihilation gamma photons. First of all, the depth at which these 511 keV gamma photons interact in the scintillator is (almost) uniformly distributed over the scintillation crystal while gamma photons resulting from common SPECT tracers mainly interact in the crystal’s top. Reconstructed hot-rod Derenzo phantom images (figure 4) showed that not including the

variable DOI in photon transport models resulted in artefacts; circularly shaped rods appeared to have a somewhat triangular shape which is probably due to the triangular detector configuration that VECTor applies. Furthermore, it was found that it is important to include the long PSF tails. The initial setting of $C = 20\%$ (meaning that only gamma photons with a probability $>20\%$ to go through the collimator were included) which is already lower than what is commonly used for SPECT image reconstruction (van der Have *et al* 2008), was far from optimal. Lowering the cut off lead to large visual improvements in both hot-rod Derenzo phantoms and uniform syringe images (figures 4 and 7). Furthermore, a more quantitative analysis showed that such a low cut off resulted in much better contrast between different rods in the hot-rod Derenzo phantom I at an equal noise level than the initial cut off of 20%. Also, much less activity was wrongly reconstructed outside the uniform syringe when a lower cut off was used.

As also indicated in this paper, lowering the cut off has its disadvantages in terms of the computational speed of image reconstruction. Image reconstruction time depends on multiple factors such as number of bed positions, number of iterations required, voxel size and available computer. To give an idea of typical times, for $C = 5\%$ reconstruction of the cardiac scan, focused bone scan and whole body bone scan shown in figure 8 took 1.5, 2 and 20 min per iteration respectively on our 48-core computer (AMD Opteron 6344 2.60 GHz Processors). For $C = 1\%$ these iteration times increased to 35, 37 and 146 min. We have recently introduced new accelerated image reconstruction algorithms, which automatically and locally adapt the number of subsets to the count level of the image (Count-regulated OSEM (Vaissier *et al* 2013), Similarity-regulated OSEM (Vaissier *et al* 2015)). In SPECT, these algorithms allowed for the safe use of a large number of subsets (e.g. 128) leading to accelerated image reconstruction. In the near future, we will validate these algorithms for reconstruction of PET images. Furthermore, we will test if we can model the long PSF tails (which are slowly varying in space) on a coarser voxel grid than the central parts of the PSFs. These low-frequency components could then only be used in the forward step of image reconstruction in a dual-matrix approach which will lead to additional speed ups. Such accelerated image reconstruction algorithms combined with next generation specialized hardware and dedicated programming are expected to make image reconstruction with even lower values of C feasible. In this paper it was already shown that a value of $C = 0.5\%$ further reduced levels of activity reconstructed in the background compared to $C = 1\%$. Furthermore, figure 3 suggests that lower levels of C may still further improve images as larger parts of the flux can then be modelled.

Note that in this paper we have restricted our quantitative analyses to a hot-rod Derenzo phantom and a uniformly filled syringe, as these phantoms are readily available and often used to assess system performance. In animal scans, such as the mouse images shown in this paper, one is often concerned with recovering features in a non-zero background. Studying image characteristics in phantoms that also contain structures in a non-zero background could be an interesting topic of future research.

5. Conclusion

New image reconstruction software incorporating accurate modelling of annihilation gamma photon transport was presented for reconstruction of pinhole PET images. The new software does not require calibration measurements additional to the ^{99m}Tc point source measurements that are routinely done for SPECT image reconstruction on the same device. Modelling certain physical effects specific to high-energy gamma photon transport significantly improved images; including a model for variable DOI in the gamma detector was necessary to avoid

triangular artefacts while including long PSF tails improved contrast-over-noise characteristics and levels of noisy background activity of reconstructed phantom and mouse images.

Acknowledgments

We thank R Ramakers for performing the mouse scans shown in this paper. This research was cofinanced by grant PID06015 under the program Pieken in the Delta Zuidvleugel of the Ministry of Economic Affairs and Provincie Zuid-Holland, The Netherlands.

References

- Agostinelli S *et al* 2003 GEANT4—a simulation toolkit *Nucl. Instrum. Methods A* **506** 250–303
- Allison J *et al* 2006 Geant4 developments and applications *IEEE Trans. Nucl. Sci.* **53** 270–8
- Beekman F J 2011 Focused pinhole gamma detection device *European Patent* no. EP2073039 2009 *US Patent* US20090159802
- Beekman F J, de Jong H W A M and van Geloven S 2002 Efficient fully 3D iterative SPECT reconstruction with Monte Carlo-based scatter compensation *IEEE Trans. Med. Imaging* **21** 867–77
- Beekman F J, van der Have F, Vastenhouw B, van der Linden A J, van Rijk P P, Burbach J P and Smidt M P 2005 U-SPECT-I: a novel system for submillimeter-resolution tomography with radiolabeled molecules in mice *J. Nucl. Med.* **46** 1194–200
- Beque D, Nuyts J, Bormans G, Suetens P and Dupont P 2003 Characterization of pinhole SPECT acquisition geometry *IEEE Trans. Med. Imaging* **22** 599–612
- Beque D, Nuyts J, Suetens P and Bormans G 2005 Optimization of geometrical calibration in pinhole SPECT *IEEE Trans. Med. Imaging* **24** 180–90
- Branderhorst W, Vastenhouw B and Beekman F J 2010 Pixel-based subsets for rapid multi-pinhole SPECT reconstruction *Phys. Med. Biol.* **55** 2023–34
- Branderhorst W, Vastenhouw B, van der Have F, Blezer E L A, Bleeker W K and Beekman F J 2011 Targeted multi-pinhole SPECT *Eur. J. Nucl. Med.* **38** 552–61
- Chen Y-C, Furenlid L R, Wilson D W and Barrett H H 2005 *Small-Animal SPECT Imaging* ed M A Kupinski and H H Barrett (New York: Springer) pp 195–201
- Constantinescu C C and Mukherjee J 2009 Performance evaluation of an inveon PET preclinical scanner *Phys. Med. Biol.* **54** 2885–99
- de Swart J, Chan H S, Goorden M C, Morgenstern A, Bruchertseifer F, Beekman F J, de Jong M and Konijnenberg M W 2016 Utilizing high energy gamma photons for high-resolution ^{213}Bi SPECT in mice *J. Nucl. Med.* **57** 486–92
- Defrise M, Vanhove C and Nuyts J 2008 Perturbative refinement of the geometric calibration in pinhole SPECT *IEEE Trans. Med. Imaging* **27** 204–14
- Furenlid L R, Wilson D W, Chen Y C, Kim H, Pietraski P J, Crawford M J and Barrett H H 2004 FastSPECT II: a second-generation high-resolution dynamic SPECT imager *IEEE Trans. Nucl. Sci.* **51** 631–5
- Gieles M, de Jong H W A M and Beekman F J 2002 Monte Carlo simulations of pinhole imaging accelerated by kernel-based forced detection *Phys. Med. Biol.* **47** 1853–67
- Goertzen A L *et al* 2012 NEMA NU 4-2008 comparison of preclinical PET imaging systems *J. Nucl. Med.* **53** 1300–9
- Goorden M C and Beekman F J 2010 High-resolution tomography of positron emitters with clustered pinhole SPECT *Phys. Med. Biol.* **55** 1265–77
- Goorden M C, van der Have F, Kreuger R and Beekman F J 2011 An efficient simulator for pinhole imaging of PET isotopes *Phys. Med. Biol.* **56** 1617–34
- Goorden M C, van der Have F, Kreuger R, Ramakers R M, Vastenhouw B, Burbach J P H, Booij J, Molthoff C F M and Beekman F J 2013 VECTor: a preclinical imaging system for simultaneous submillimeter SPECT and PET *J. Nucl. Med.* **54** 306–12
- Herrmann K, Dahlbom M, Nathanson D, Wei L, Radu C, Chatzioannou A and Czernin J 2013 Evaluation of the Genisys4, a bench-top preclinical PET scanner *J. Nucl. Med.* **54** 1162–7

- Hesterman J Y, Kupinski M A, Furenlid L R, Wilson D W and Barrett H H 2007 The multi-module, multi-resolution system (M(3)R): a novel small-animal SPECT system *Med. Phys.* **34** 987–93
- Hudson H M and Larkin R S 1994 Accelerated image-reconstruction using ordered subsets of projection data *IEEE Trans. Med. Imaging* **13** 601–9
- Hutton B F, Hudson H M and Beekman F J 1997 A clinical perspective of accelerated statistical reconstruction *Eur. J. Nucl. Med.* **24** 797–808
- Ivashchenko O, van der Have F, Villena J L, Groen H C, Ramakers R M, Weinans H H and Beekman F J 2014 Quarter-millimeter-resolution molecular mouse imaging with U-SPECT⁺ *Mol. Imaging* **13** 1–8 (PMID: [25429783](#))
- Kamphuis C, Beekman F J, van Rijk P P and Viergever M A 1998 Dual matrix ordered subsets reconstruction for accelerated 3D scatter compensation in single-photon emission tomography *Eur. J. Nucl. Med.* **25** 8–18
- King M A, deVries D J, Pan T S, Pretorius P H and Case J A 1997 An investigation of the filtering of TEW scatter estimates used to compensate for scatter with ordered subset reconstructions *IEEE Trans. Nucl. Sci.* **44** 1140–5
- Leahy R and Byrne C 2000 Recent developments in iterative image reconstruction for PET and SPECT *IEEE Trans. Med. Imaging* **19** 257–60
- Leahy R M and Qi J Y 2000 Statistical approaches in quantitative positron emission tomography *Stat. Comput.* **10** 147–65
- Li J Y, Jaszczak R J, Wang H L, Greer K L and Coleman R E 1993 Determination of both mechanical and electronic shifts in cone-beam spect *Phys. Med. Biol.* **38** 743–54
- Liu Z L, Kastis G A, Stevenson G D, Barrett H H, Furenlid L R, Kupinski M A, Patton D D and Wilson D W 2002 Quantitative analysis of acute myocardial infarct in rat hearts with ischemia-reperfusion using a high-resolution stationary SPECT system *J. Nucl. Med.* **43** 933–9
- Metzler S D, Bowsher J E, Greer K L and Jaszczak R J 2002 Analytic determination of the pinhole collimator's point-spread function and RMS resolution with penetration *IEEE Trans. Med. Imaging* **21** 878–87
- Metzler S D, Greer K L and Jaszczak R J 2005 Determination of mechanical and electronic shifts for pinhole SPECT using a single point source *IEEE Trans. Med. Imaging* **24** 361–70
- Metzler S D and Jaszczak R J 2006 Simultaneous multi-head calibration for pinhole SPECT *IEEE Trans. Nucl. Sci.* **53** 113–20
- Miller B W, Van Holen R, Barrett H H and Furenlid L R 2012 A system calibration and fast iterative reconstruction method for next-generation SPECT imagers *IEEE Trans. Nucl. Sci.* **59** 1990–6
- Miwa K, Inubushi M, Takeuchi Y, Katafuchi T, Koizumi M, Saga T and Sasaki M 2015 Performance characteristics of a novel clustered multi-pinhole technology for simultaneous high-resolution SPECT/PET *Ann. Nucl. Med.* **29** 460–6
- Nagy K, Toth M, Major P, Patay G, Egri G, Haggkvist J, Varrone A, Farde L, Halldin C and Gulyas B 2013 Performance evaluation of the small-animal nanoscan PET/MRI system *J. Nucl. Med.* **54** 1825–32
- Noo F, Clackdoyle R, Mennessier C, White T A and Roney T J 2000 Analytic method based on identification of ellipse parameters for scanner calibration in cone-beam tomography *Phys. Med. Biol.* **45** 3489–508
- Qi J Y and Leahy R M 2006 Iterative reconstruction techniques in emission computed tomography *Phys. Med. Biol.* **51** R541–78
- Rizo P, Grangeat P and Guillemaud R 1994 Geometric calibration method for multiple-head cone-beam spect system *IEEE Trans. Nucl. Sci.* **41** 2748–57
- Smith M F and Jaszczak R J 1998 An analytic model of pinhole aperture penetration for 3D pinhole SPECT image reconstruction *Phys. Med. Biol.* **43** 761–75
- Spinks T J, Karia D, Leach M O and Flux G 2014 Quantitative PET and SPECT performance characteristics of the albira trimodal pre-clinical tomograph *Phys. Med. Biol.* **59** 715–31
- Vaissier P E B, Beekman F J, van der Have F and Goorden M C 2015 Improved regulated OSEM reconstruction with adaptive resolution recovery *Phys. Med. Biol.* submitted
- Vaissier P E B, Goorden M C, Taylor A B and Beekman F J 2013 Fast count-regulated OSEM reconstruction with adaptive resolution recovery *IEEE Trans. Med. Imaging* **32** 2250–61
- Vaissier P E B, Goorden M C, Vastenhouw B, Van der Have F, Ramakers R M and Beekman F J 2012 Fast spiral SPECT with stationary γ -cameras and focusing pinholes *J. Nucl. Med.* **53** 1292–9
- van der Have F, Ivashchenko O, Goorden M C, Ramakers R M and Beekman F J 2015 High-resolution iodine-131 SPECT imaging in mice *IEEE NSS-MIC (31 October–7 November, San Diego)*

- van der Have F, Vastenhouw B, Ramakers R M, Branderhorst W, Krah J O, Ji C, Staelens S G and Beekman F J 2009 U-SPECT-II: an ultra-high-resolution device for molecular small-animal imaging *J. Nucl. Med.* **50** 599–605
- van der Have F, Vastenhouw B, Rentmeester M and Beekman F J 2008 System calibration and statistical image reconstruction for ultra-high resolution stationary pinhole SPECT *IEEE Trans. Med. Imaging.* **27** 960–71
- Vastenhouw B and Beekman F 2007 Submillimeter total-body murine imaging with U-SPECT-I *J. Nucl. Med.* **48** 487–93
- Walker M D, Goorden M C, Dinelle K, Ramakers R M, Blinder S, Shirmohammad M, van der Have F, Beekman F J and Sossi V 2014 Performance assessment of a preclinical pet scanner with pinhole collimation by comparison to a coincidence-based small-animal PET scanner *J. Nucl. Med.* **55** 1368–74
- Weber D A *et al* 1994 Pinhole SPECT—an approach to *in vivo* high-resolution SPECT imaging in small laboratory-animals *J. Nucl. Med.* **35** 342–8
- Weissleder R, Ross B D, Rehemtulla A and Gambhir S S 2010 *Molecular Imaging: Principles and Practice* (Shelton, CT: People's Medical)
- Wu C, de Jong J R, van Andel H A G, van der Have F, Vastenhouw B, Laverman P, Boerman O C, Dierckx R A J O and Beekman F J 2011 Quantitative multi-pinhole small-animal SPECT: uniform versus non-uniform Chang attenuation correction *Phys. Med. Biol.* **56** N183–93
- Zeng G L and Gullberg G T 1992 Frequency-domain implementation of the 3D geometric point response correction in spect imaging *IEEE Trans. Nucl. Sci.* **39** 1444–53